Evanescent wave cavity ring-down spectroscopy for ultra-sensitive chemical detection

Andrew C. R. Pipino*

Experimental Chemical Kinetics Group
Physical and Chemical Properties Division
Chemical Science and Technology Laboratory
National Institute of Standards and Technology
Gaithersburg, Maryland 20899

ABSTRACT

A new technology will be described which extends the cavity ring-down optical absorption technique to condensed matter by using a miniature, high-finesse, monolithic, total-internal-reflection-ring resonator. Evanescent waves that are generated by total-internal reflection permit input and ouput coupling by photon tunneling and probe the presence of absorbing species at a cavity facet. The TIR-ring design permits broadband cavity ring-down measurements of adsorbates, thin films, and liquids by eliminating the use of multilayer coatings. The basic sensing concept will first be reviewed by describing recent experiments employing a non-ring prototype in which a totally reflecting element was incorporated in a conventional ring-down cavity. The basic design issues for miniature TIR-ring cavities will then be briefly reviewed along with some numerical results obtained using a wave optics model that show the magnitude of different optical losses as a function of cavity size. A competition between losses results in an optimum size for chemical detection which occurs when the round-trip loss of the "empty" cavity is minimized. The first experimental results will be presented for a square (7 mm x 7 mm x 5 mm), fused-silica TIR-ring cavity for which the theoretically predicted photon decay time has been achieved.

Keywords: cavity ring-down, evanescent waves, optical absorption, thin films, surface spectroscopy, fused silica, miniature cavity

1. INTRODUCTION

Cavity ring-down spectroscopy[1] (CRDS) uses the photon lifetime in a high-finesse optical cavity to measure optical absorption under conditions of low number density or small absorption cross section. Although CRDS has yielded a variety of successes for gas phase studies, the method has only recently been extended to condensed matter[2-3]. In gas-phase CRDS, the cavity is typically formed from a pair of narrowband, ultra-high reflectivity dielectric mirrors, arranged to form a stable optical resonator as shown in Figure 1. A light pulse, which enters the cavity through a weakly transmissive cavity mirror, circulates with a e^{-1} lifetime or "ring-down time" given by,

$$\tau(\omega) = \frac{t_r}{2(1 - R(\omega)) + 2\alpha(\omega)NL} \qquad (1)$$

where t_r is the round-trip transit time for light in the cavity of length L, α and N are the absorption coefficient and number density, respectively, and 1- R(ω) accounts for the intensity loss arising from imperfect mirror reflectivity.

*NRC postdoctoral Associate/NIST 1995-1997; E-mail: andrew.pipino@nist.gov

Part of the SPIE Conference on Advanced Sensors and Monitors for Process Industries and the Environment
Boston, Massachusetts • November 1998 SPIE Vol. 3535 • 0277-786X/99/$10.00

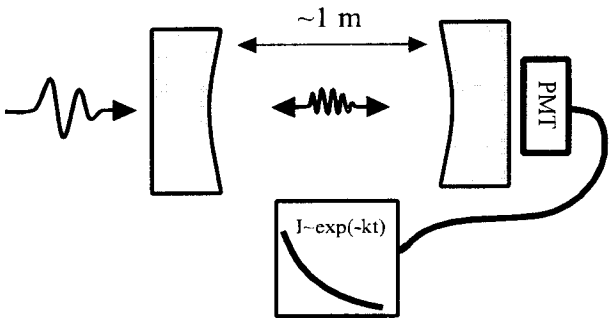

Figure 1. The basic CRDS experiment is depicted. A light pulse is injected into the cavity through a weakly transmissive mirror. The exponentially decaying intensity of the injected pulse is characterized by fitting the digitized output of the photomultiplier tube (PMT) to an exponential function. The decay time, given by Eq. 1, is highly sensitive to mirror losses and absorption by gases between the mirrors. The CRDS technique has been applied previously only to gas diagnostics.

A complete measurement of absorption is accomplished with a single light pulse, thereby eliminating errors introduced by pulse-to-pulse fluctuations of the source. The minimum detectable absorbance change for any cavity ring-down measurement is determined by the product of the empty cavity loss-per-pass, $\mathcal{L}_0$, and the minimum detectable relative change, $\Delta\tau/\tau$, in the ring-down time[4] or

$$(\alpha L)_{\min} = \mathcal{L}_0\left(\frac{\Delta\tau}{\tau}\right) = (1-R)\left(\frac{\Delta\tau}{\tau}\right) \qquad (2)$$

where the last equality holds for the cavity of Figure 1. This expression factors the detection limit into a cavity dependent term and an instrumentation dependent term. The sensitivity of CRDS typically equals or exceeds that of common modulation techniques and may eventually facilitate routine achievement of shot-noise limited absorption measurements.

Extension of CRDS to condensed matter requires cavity designs that provide a small round-trip cavity loss and a well-defined relationship between the ring-down time and sample absorption. A broadband cavity would also clearly be advantageous. These complications are largely resolved through the use of total-internal reflection which has many advantages for CRDS. If non-specular losses can be neglected[5], the efficiency of TIR is reduced from unity only by surface roughness scattering, which can be made small by superpolishing techniques. TIR is also inherently broadband and the accompanying evanescent wave, which arises as a natural consequence of TIR, is an effective spectroscopic probe for surface, thin-film, and liquid-phase studies, forming the basis for attenuated total reflection (ATR) spectroscopy[6]. Furthermore, in the case of a TIR-ring cavity the presence of evanescent waves permits control of resonator input and output coupling through photon tunneling[7]. By constructing a CRD cavity that incorporates intra-cavity TIR, the benefits of an evanescent wave technique can be combined with the enhanced sensitivity of CRDS to provide a significant advancement in surface and thin-film diagnostics.

In the following, previous work on extending CRDS to condensed matter is briefly reviewed[2,3]. The first evanescent wave CRDS experiment used a variant of the standard CRDS cavity that incorporated a low-loss, totally reflecting optical element; a small fraction of a monolayer of adsorbed iodine was detected[2]. Although this cavity design suffers from narrow bandwidth and is not easily interfaced to ordinary reaction chambers, it serves the purpose of verifying the sensing concept. The TIR-ring cavity design, which overcomes these remaining restrictions, is then described and basic design criteria are briefly reviewed[3]. Wave optics calculations that show the existence of an optimum cavity size that maximizes chemical detection sensitivity are also discussed. Finally, the first experimental results are shown for a square TIR-ring cavity that was fabricated from fiber-optic-grade fused silica. The measured ring-down time for this cavity is equal to the theoretically predicted value within experimental error.

2. INITIAL DEMONSTRATION OF THE SENSING CONCEPT

To establish the feasibility of combining TIR with CRDS a cavity was constructed which forms a stable resonator with intra-cavity TIR as shown in Figure 2. The cavity consists of two concave, dielectric mirrors (Newport 10CV00-SR.30F, 1 m radius of curvature) with reflectivity of ~99.99% at 620 nm and a fused-silica (Corning 7940) Pellin-Broca prism (CVI Laser) which has a 632.8 nm design wavelength. The output of an excimer-pumped, dye laser using Sulforhodamine 640 was passed through a Glan-laser prism prior to entering the cavity to provide horizontally polarized light with an extinction ratio of $<10^{-3}$. The cavity output was detected by a photomultiplier tube located behind the second mirror. The output of the PMT was digitized by an 8-bit, 500 megasamples/s oscilloscope with a 25 MHz bandwidth-limiting filter and transferred to a microcomputer. After filtering, smooth, single-exponential decay waveforms were obtained for p-polarized input. Typically, a 0.2% standard deviation in the decay time was found for data in which each point was a 25 shot average. A representative, unfiltered ring-down decay is shown as an inset in Figure 2.

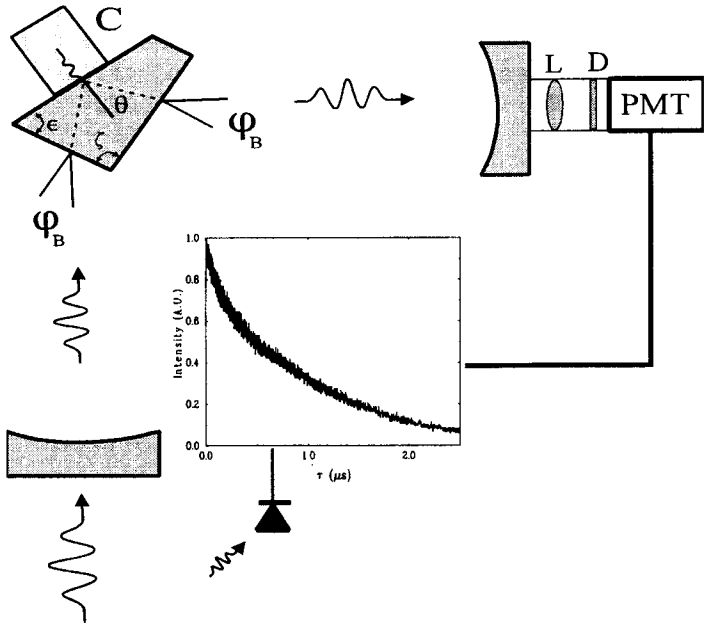

Figure 2. A low-loss optical cavity is shown which incorporates intra-cavity TIR. Light enters and exits the Pellin-Broca prism at Brewster's angle to minimize Fresnel reflection losses. The cavity yields a minimum detectable absorbance change of ~26 ppm, based on the round-trip loss of 6400 ppm and a minimum detectable decay time change of $\Delta\tau/\tau=0.004$. The presence of I_2 in the cell **C** results in adsorption of I_2 at the TIR surface. A detection limit of 0.04 monolayers of I_2 has been achieved with this system. The inset shows an unfiltered ring-down trace for a single shot. L=lens, D=diffuser. The scope is triggered with a photodiode.

Intra-cavity TIR introduces new intrinsic losses that are not present in conventional CRDS cavities. The photon decay time for the cavity of Figure 2 can be expressed in terms of the round-trip time, t_r, and the round-trip cavity losses according to

$$\tau(\omega)=\frac{t_r}{2(1-R)+\mathcal{L}_{bulk}+\mathcal{L}_{surf}+\mathcal{L}_{pol}+2\Gamma\sigma(\omega)N_s} \qquad (3)$$

where R is mirror reflectivity, $\mathcal{L}_{bulk}$ is the prism bulk attenuation, $\mathcal{L}_{surf}$ is the prism surface scattering loss, $\mathcal{L}_{pol}$ is the total polarization-dependent loss, and $\sigma(\omega)$, Γ, and N_s are the absorption cross-section, surface field intensity enhancement, and number density for the adsorbed species, respectively. The bulk attenuation is estimated to be 640

ppm per round trip at 625 nm[8]. The surface scattering loss per round trip that is introduced by the Pellin-Broca prism can be calculated from[9]

$$\mathcal{L}_{surf} = 2\sum_{i=1}^{3}\mathcal{L}_i = 2\sum_{i=1}^{3}\left(\frac{4\pi n_i \sigma_{RMS}\cos\theta_i}{\lambda_0}\right)^2 \qquad (4)$$

where $\mathcal{L}_i$ is the surface scattering loss per surface, σ_{RMS} is the root-mean-square (rms) surface roughness, n_i is the incident-medium index of refraction, θ_i is the angle of incidence, and λ_o is the vacuum wavelength. From Eq. 4 the round-trip surface scattering loss is calculated to be 5.4 ppm for the superpolished prism with σ_{RMS}=0.05 nm. A 418 ppm loss is estimated for the prism prior to superpolishing based on a measured σ_{RMS}=0.44 nm.

When bulk attenuation, surface scattering, and mirror losses are made sufficiently small, the intrinsic cavity loss is largely determined by polarization effects. The Pellin-Broca prism provides high transmission for p-polarized light near the design wavelength, since light enters and exits the prism at or near Brewster's angle. The total polarization loss can be decomposed into in-plane and out-of-plane losses with respect to the plane of the cavity according to

$$\mathcal{L}_{pol} = \mathcal{L}^{\parallel}_{pol} + \mathcal{L}^{\perp}_{pol}, \qquad (5)$$

where $\mathcal{L}^{\parallel}_{pol}$ arises from inaccuracies in the angles ζ and ϵ in Figure 2 that introduce deviations from concurrent Brewster angle input and output, and $\mathcal{L}^{\perp}_{pol}$ arises from deviations in the plane of polarization from the ideal p-polarized state which are introduced by pyramidal error and the depolarizing properties of the optical elements. The in-plane loss per round trip can be estimated by assuming an incident plane wave, expanding the reflectivity for p-polarized light in a Taylor series around the Brewster angle, and truncating after the first non-zero term to obtain

$$\mathcal{L}^{\parallel}_{pol} \approx 2\sum_{i}^{\theta_B,\theta_P}\left|\frac{\partial R_{\parallel}(\theta_i)}{\partial\theta}(\theta-\theta_i)\right|^2 = 2\left(\left(\frac{1-n^4}{2n^3}\right)^2(\Delta\theta_B)^2+\left(\frac{1-n^4}{2n}\right)^2(\Delta\theta_P)^2\right) = \left(\frac{1-n^4}{n}\right)^2(\Delta\chi)^2 \qquad (6)$$

where $R_{\parallel}(\theta_i)$ is the p-polarization amplitude reflectivity, $\Delta\theta_B$ and $\Delta\theta_P$ correspond to the deviations from Brewster's angle for the air/fused-silica and fused-silica/air interfaces, respectively, under optimal alignment conditions (loss limited by fabrication error), and $\Delta\chi=2\Delta\epsilon+\Delta\zeta$. Note that if the errors $\Delta\epsilon$ and $\Delta\zeta$ both lead to larger or smaller values for ζ and ϵ, the error will accumulate. The angles ζ and ϵ and pyramidal error where corrected during the superpolishing process to within ±5 arc minutes of the target values. According to Eq. 6, this leads to a maximum contribution to the round trip loss of 110 ppm, assuming maximum error accumulation. The out-of-plane polarization loss arises from stress birefringence, pyramidal error, and depolarization by the concave, multilayer dielectric mirrors which result in the generation of an s-polarization component that is efficiently rejected by the Brewster angle facets of the Pellin-Broca. If the angle of the electric field relative to the plane of the cavity is δ, the out-of-plane polarization loss is given by

$$\mathcal{L}^{\perp}_{pol} = 2\sum_{i}^{\theta_B,\theta_P}\left|R_{\perp}(\theta_i)\right|^2\sin^2\delta_i = 2\left|\frac{1-n_i^2}{1+n_i^2}\right|^2\left(\sin^2\delta_{\theta_B}+\sin^2\delta_{\theta_P}\right) \qquad (7)$$

where $R_{\perp}(\theta_i)$ is the s-state amplitude reflectivity, and θ_B,θ_P are the incident angles at the rarer→denser and

denser→rarer interfaces, respectively, where the reflectivities and polarization angles are evaluated. A detailed model could be developed for δ as a function of position in the cavity, but ultimately accurate characterization of the particular optical components is required. The contribution of stress birefringence to the total loss will be greatly reduced by using a smaller prism which is fabricated from a selected grade of material.

To quantify sensitivity, the TIR surface of the Pellin-Broca prism was exposed to I_2 vapor to monitor the adsorption process by locating a cell at the TIR facet as shown in Figure 2. Solid I_2 was added to the cell to establish a constant I_2 dosing pressure based on the solid/vapor equilibrium at constant temperature. The vapor pressure of I_2 is estimated to be 37 Pascal (0.28 Torr)[10] at the ambient temperature of 22.4 ± 0.1°C during the experiment. The cell dimensions (1.0 cm x 2.3 cm x 5.0 cm) where large compared to the sampled area so that the area being probed experienced uniform dosing conditions. It is known from the literature that adsorption of I_2 on silica at room temperature results in sub-monolayer coverage[11]. The visible absorption spectrum of I_2 adsorbed on silica was also measured and shows relatively small shifting and broadening relative to the pressure-broadened gas phase absorption spectrum. Therefore, I_2 serves as an approximate "calibration system" to evaluate the sensitivity. Exposure of the Pellin-Broca TIR surface to I_2 vapor was cycled, as shown in Figure 3 where the total cavity loss is plotted for four adsorption and desorption cycles. The step-function-like changes result from a 3 minute equilibration time following exposure or removal of the I_2 cell, during which acquisition was halted. For each adsorption or desorption phase, data were collected for 6 minutes at a 10 Hz repetition rate with 25 shots averaged per point. Results for two wavelengths, 625 nm and 660 nm, are shown, corresponding to the upper and lower waveforms, respectively. The sensitivity for probing the adsorption is greater at 625 nm compared to 660 nm. This difference arises from the difference in absorption cross-section at these wavelengths for the visible transition of I_2, which in the gas phase has an absorption maximum at 520 nm with $\alpha_{520nm} = 2.56 \times 10^{-18}$ cm^2/molecule[12]. To quantify the sensitivity of evanescent wave CRDS in the form of a minimum detectable coverage, values for the surface electric field intensity enhancement and the absorption cross-section of adsorbed I_2 are needed. Using the gas phase value for the absorption cross-section at the probe wavelength, which is estimated to be $\sigma_{625nm} = 2.5 \times 10^{-19}$ cm^2/molecule, the minimum detectable coverage of adsorbed I_2 can be estimated. The gas phase value should represents lower limit for the cross-section in the tail of the absorption that will underestimate the minimum detectable surface coverage. Therefore, assuming $N_o = 5 \times 10^{14}$ sites/cm^2 as the density of adsorption sites[11], a minimum detectable coverage is estimated to be 0.04 monolayers. These calculations utilize the maximum field enhancement factor, which is 7.4 as calculated from the Fresnel equations.

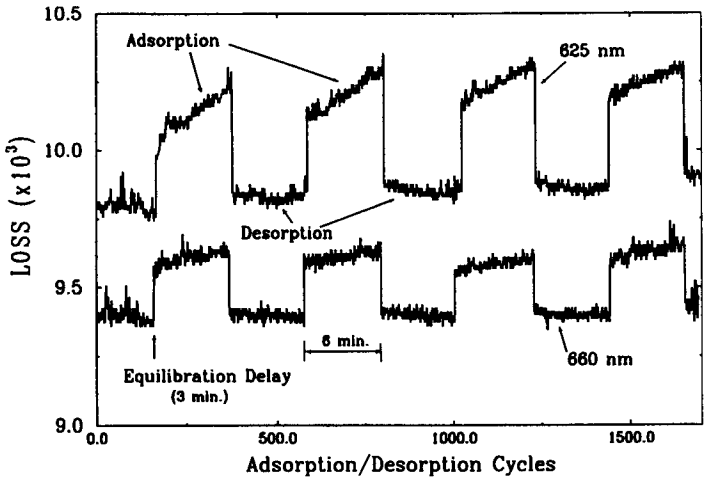

Figure 3. The adsorption of I_2 on the superpolished fused silica TIR surface is demonstrated at two wavelengths by measuring the increased cavity loss. Four typical adsorption/desorption cycles are shown to illustrate reversibility and repeatability for each wavelength. The step-like changes result from stopping the acquisition to allow equilibration. The larger response detected at 625 nm compared with 660 nm arises from the larger absorption cross-section at 625 nm. The small difference in base loss at the two wavelengths arises from the weak dependence of photon decay time on wavelength over this range.

3. MONOLITHIC TIR-RING CAVITY DESIGN

Although the cavity of Figure 2 achieved submonolayer detection with good signal-to-noise ratio, the narrow bandwidth, large polarization-dependent loss, and awkward geometry limit the range of application of the design. To circumvent these limitations, the design of Figure 4 was conceived which incorporates a monolithic, total-internal-reflection-ring cavity of regular polygonal geometry with a convex facet to induce stability for the cavity modes. Light enters or exits the resonator by photon tunneling, which can be precisely controlled by varying the gap widths between the cavity and the coupling prisms. The broadband nature of total-internal reflection eliminates the wavelength limitation imposed by dielectric mirrors. As in ordinary CRDS, the absorption spectrum is extracted by measuring the ring-down time of individual light pulses as a function of pulse carrier frequency, so that minimal error is introduced by light source fluctuations.

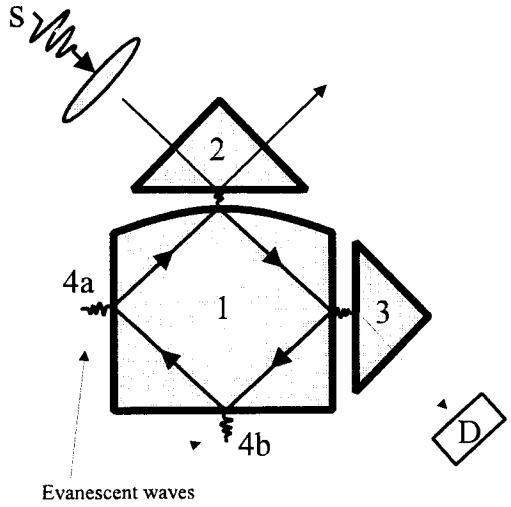

Figure 4. A miniature (<1 cm^3) polygonal, monolithic TIR-ring cavity (1) forms the basis for a novel, cavity ring-down spectrometer. Elements 2 and 3 are used to couple light into and out of the solid cavity by photon tunneling. Evanescent waves at positions 4a-b probe the surrounding medium. Measurement of the decay rate of an injected light pulse permits accurate and absolute determination of absorption over the well-defined path length established by the evanescent wave decay length. Input and output light beams can be transported by fiber-optics to remotely locate the light source (S) and detector (D). The cavity dimensions are 7 mm x 7 mm x 5 mm.

4. THEORETICAL MODEL

A wave optics model for the minicavity ring-down spectrometer permits quantitative evaluation of performance and design optimization. Wave optics, as opposed to geometric optics, must be used since diffraction effects are of critical importance. The basic design criteria for a general polygonal resonator are reviewed briefly below. Numerical results for an square-ring cavity are then presented which demonstrate the optimization procedure.

4.1 Design criteria

4.1.1 General considerations

As discussed previously, the minimum detectable absorbance change in CRDS can be expressed as the product of the intrinsic cavity losses and the minimum detectable relative change in the photon decay time, or $(\Delta\tau/\tau)\mathcal{L}_o$. The TIR-ring cavity design that will yield maximum sensitivity arises from an interplay between several factors. Since the round-trip time, bulk attenuation, and diffraction losses are linked to the size of the cavity, the optimal resonator size will be determined by minimization of loss, as long as a sufficiently long decay time is achieved for accurate digitization. By analogy with Eq.1, the photon decay time in a monolithic, TIR-ring cavity

with n facets is given by

$$\tau(\omega) = \frac{t_r}{\mathfrak{L}_{bulk} + \mathfrak{L}_{surf} + \mathfrak{L}_{diff} + \mathfrak{L}_{coup} + \mathfrak{L}_{nspec} + (n-2)\sum_i \sigma_i(\omega)\int_0^{d_e} N_i(\xi)d\xi} \tag{8}$$

where $\mathfrak{L}_{bulk}$, $\mathfrak{L}_{surf}$, $\mathfrak{L}_{diff}$, $\mathfrak{L}_{coup}$, $\mathfrak{L}_{nspec}$ are the round-trip bulk, surface scattering, diffraction, coupling, and nonspecular losses, respectively, and d_e is the effective thickness sampled by the evanescent wave. In Eq. 8, two TIR surfaces are assumed to serve as coupling ports, while the remaining n-2 surfaces sample the surrounding medium. For an n-sided ring resonator of refractive index n_i, the round-trip time is simply

$$t_r = n_i L_{rt}/c = 2n(n_i/c)r_o\sin(\pi/n) \tag{9}$$

where r_o is the inscribed-circle radius of the associated polygon and L_{rt} is the round-trip physical path length, which approaches $2\pi r_o$ in the limit as $n\to\infty$. The dependence of the photon decay time on the size of the cavity is incorporated directly in t_r and $\mathfrak{L}_{bulk}$, while $\mathfrak{L}_{diff}$ depends on cavity size through the stability factors and the presence of apertures associated with the finite facet dimensions.

4.1.2 Bulk attenuation

For a resonator that is fabricated from a highly transparent material, the loss-per-pass due to bulk attenuation is well-approximated by

$$\mathfrak{L}_{bulk} = 2\alpha r_o n\sin(\pi/n) \tag{10}$$

where α is the bulk attenuation coefficient. Note from Eqs. 8, 9, 10 that as the size of the resonator is increased, such that bulk attenuation dominates, the photon decay time asymptotically approaches a constant value. An increase in cavity size beyond the point at which a sufficiently long decay time is obtained for accurate digitization, will only increase the minimum detectable absorbance change (decrease sensitivity). In the visible and near-IR, fiber-optic-grade fused-silica and certain borosilicate glasses have an attenuation of 20 dB/km (46 ppm cm^{-1}) or less. In the mid-infrared, several fluoride glasses have extremely high transmission (<1 dB/km), which would permit vibrational fundamentals to be probed with extremely high sensitivity[13].

4.1.3 Surface scattering loss

When bulk attenuation is sufficiently small (~50 ppm/pass), surface scattering can become significant. The round-trip surface scattering loss can be calculated from

$$\mathfrak{L}_{surf} \approx \left(\frac{4\pi n_i \sigma_{RMS}\sqrt{n}\cos\theta_i}{\lambda_0}\right)^2 = \left(\frac{4\pi n_i \sigma_{RMS}\sqrt{n}\sin(\pi/n)}{\lambda_0}\right)^2 \tag{11}$$

where σ_{RMS} is the root-mean-square surface roughness, λ_0 is the vacuum wavelength, and the angle of incidence, $\theta_i = \pi(n-2)/2n$, has been generalized for an n-sided, regular polygonal resonator. According to Eq. 11, the scattering loss for σ_{RMS}~0.05 nm is below 5 ppm per round-trip at 620 nm for a square, fused-silica resonator with θ_i=45°. The strong incident-angle dependence in Eq. 11 also results in a reduction of the round-trip surface scattering loss for resonators with larger values of n, corresponding to larger angles of incidence, despite the increased number of total reflections. However, the reduction in surface scattering loss with increasing angle of incidence is counteracted by an increase in diffraction losses arising from aperturing by the cavity facets.

4.1.4. Resonator stability

By definition, a stable resonator supports low-diffraction-loss modes which are self-reproducing[14]. As in the case of a linear resonator constructed from plane-parallel mirrors, a polygonal ring resonator consisting of n plane-parallel mirrors is borderline unstable resulting in large diffraction losses since no refocussing occurs. The presence of a single convex facet induces stability for a ring resonator, thereby substantially diminishing diffraction losses. If the convex facet has a spherical radius, the effective focal lengths and mode waist sizes in the tangential and sagittal planes are different, resulting in an astigmatic resonator.

4.1.5 Frequency selectivity

The role of cavity transverse and longitudinal mode structure in CRDS has been discussed[15,16]. The discrete mode spectrum could result in loss of spectral information if an absorption line is located between mode frequencies or inefficient coupling if the bandwidth of the pulsed excitation source is narrow compared to the mode spacing. The polarization-dependent mode frequencies $\omega_{q,m,k}$ for an n-sided monolithic, TIR-ring cavity are given by[14]

$$\omega_{q,m,k}^{s,p} = \frac{c}{n_i L_{rt}} \left[2\pi q + \phi_x^k + \phi_y^m - \sum_{j=1}^{n} \gamma_{s,p}^{(j)} \right] \qquad (12)$$

where ϕ_x and ϕ_y are the transverse mode-dependent Guoy phase-shifts and the $\gamma^{(j)}$ are the polarization-dependent TIR phase-shifts. Although the broad absorption lines typically associated with condensed matter spectroscopy reduce the chances that spectral information will be lost, the large free-spectral range implied by Eq.12 for small cavities could result in inefficient coupling if ~10 ns-pulse width excitation sources, which are common in CRDS, are applied in a minicavity experiment. To reduce the complications associated with a large free-spectral range, a nondegenerate cavity with intentional mode-mismatching can be used to excite a quasi-continuum of transverse modes within the longitudinal mode free spectral range. Mode-mismatching may be an important strategy in TIR-ring cavity CRDS to assure efficient coupling when relatively narrowband sources are used. This strategy influences the minimum useful cavity size, since the larger divergence high-order modes must experience essentially the same ring-down time as the fundamental mode.

4.1.6 Input and output coupling

As shown in Fig. 4, the modes of a TIR-ring cavity can be excited by photon tunneling, i.e. when totally reflecting prisms are placed in close proximity to the resonator such that the evanescent field is phase-matched to the resonator modes. Although the presence of any radiative channel inherently degrades finesse, photon tunneling provides precise control of coupling efficiency and the dependence of photon-tunneling on the gap-width is well-known[7]. When the gap width between the coupling element and the resonator is on the order of a wavelength, strong or moderate coupling efficiency is obtained with a concomitant degradation of finesse. For gap-widths of several wavelengths, coupling efficiency plateaus as the weak-coupling, unperturbed finesse limit is asymptotically approached. For CRDS with a TIR-ring cavity, operation in the weak coupling regime permits sufficient light to enter the cavity without incurring coupling losses that exceed the sum of other losses.

4.1.7 Nonspecular effects

Nonspecular losses[5] arise when a finite diameter beam undergoes total reflection in the vicinity of the critical angle. Because of diffraction, a finite beam diameter implies a distribution of angles of incidence, with an inverse proportionality between beam diameter and distribution width. Since the Fresnel reflection coefficients are derived strictly for a single plane wave with a given angle of incidence, the reflection of a finite beam cannot be expressed by a single Fresnel reflection coefficient. Instead, each component in the angular spectrum experiences a different phase and amplitude modification, resulting in nonspecular phenomena. For an angle of incidence that exceeds the critical angle, θ_c, by at least 1°, a loss of below 1 ppm is found for a Gaussian beam with a diameter of ~40μm at 600 nm, suggesting that nonspecular transmission loss will be small relative to other sources of loss as long as the angle of incidence is not in the immediate vicinity of the critical angle.

4.1.8 Evanescent wave absorption

The extent of evanescent wave absorption is a function of the angle of incidence and the index discontinuity at the interface as well as the absorption coefficient of the ambient medium. This dependence is incorporated into the "effective thickness", d_e, which yields a Beer-Lambert-like law for evanescent wave spectroscopy[6]. As the angle of incidence approaches the critical angle or as the index discontinuity is reduced, the effective thickness increases thereby augmenting sensitivity through an increase in path length as well as an enhancement of the local electric field. For a TIR-ring cavity with n-sides, the effective thickness is then connected to the ring-down time through Eq. 8, where the integral allows for variation of concentration with position. A circulating beam can be sustained by TIR when the angle of incidence for the beam center, given by $\theta_i = \pi(n-2)/2n$, exceeds the critical angle, $\vartheta_c = \sin^{-1}(n_o/n_i)$. Therefore, a discrete set of allowed angles of incidence exists for a given index discontinuity. The incident angle that is closest to the critical angle will provide maximum sensitivity and the smallest value of n. Since total reflection is not frustrated by films that are thin relative to the evanescent wave decay length regardless of the film refractive index, the simplest resonator design that supports stable modes in vacuum can be used for thin-film diagnostics. For bulk materials, the optimum resonator geometry will depend on the index discontinuity. The value of n must be selected to prevent frustrating the total reflection or incurring losses due to nonspecular effects as θ_i approaches θ_c. When n is increased to compensate for a decreasing index discontinuity, detection sensitivity is enhanced due to the larger number of total reflections, although the resulting resonator may present a greater fabrication challenge.

4.2 Computational results: Optimum cavity size

A TIR-ring cavity implementation of CRDS becomes feasible only if appreciable photon decay times can be obtained to permit accurate digitization. Photon decay times on the order of one microsecond, which are commonly encountered in conventional CRDS, can be accurately digitized to provide a minimum detectable relative change in the decay time of $\Delta\tau/\tau \sim 0.2\%$ or better. As stated previously, the resonator design that minimizes loss, while providing a sufficiently long decay time to achieve maximum digitization accuracy, will be optimal. A minimum in the intrinsic loss as a function of L_{rt} will exist, which arises from the competition between bulk and diffractive losses for chosen excitation conditions. Figure 5 shows the results of calculations that permit the

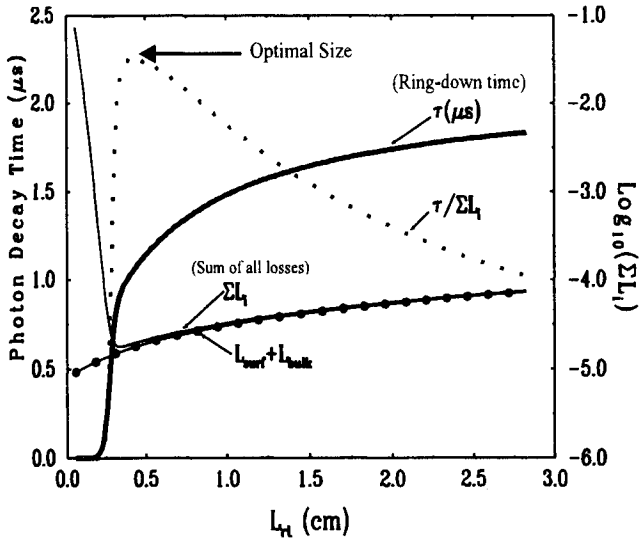

Figure 5. An optimal cavity size is found, based on selected mode-mismatching conditions, for a square, fused-silica TIR-ring cavity. The heavy, solid curves describe the photon decay time as a function of L_{rt}. The long-dashed curve and line demarked by solid circles, correspond to the right-hand-side axis and describe the total loss and the sum of bulk and surface losses, respectively. The photon decay time is seen to increase rapidly as diffraction losses decline and to asymptotically approach a constant value in the limit of large L_{rt}. The total loss function displays a minimum at which the sensitivity for detecting small absorbance changes will be maximized. The dotted line corresponds to the ratio of the round-trip time to the square of the cavity losses, which provides a measure of sensitivity. This function is plotted for relative comparison only and does not correspond to either ordinate.

determination of an optimum cavity size. The ring-down time (heavy solid line) is shown as a function of L_{rt} for a fused-silica square resonator. The total system loss (thin solid line), including bulk, surface, diffractive (with mode-mismatching), and coupling losses, and the sum of surface plus bulk losses (solid circles), are also shown, corresponding to the right-hand axis. Note that the photon decay time increases sharply as diffraction losses

decrease to yield decay times that are on the order of a microsecond. As L_{rt} is increased further the ring-down time approaches a constant value. The rapid rise in τ time occurs over the range of L_{rt} where the total system loss minimizes. The value of L_{rt} that provides the smallest total system loss will provide the lowest detection limit. Also shown in Figure 5 for relative comparison is the ratio of the photon decay time to the total system loss (dotted curves), which is proportional to the derivative of the photon decay time with respect to total loss. This function, which provides a measure of sensitivity, shows a maximum in the vicinity of the total loss minimum. An optimum value for the cavity size therefore exists that minimizes the total intrinsic loss, while providing appreciable photon decay times. Calculations for the case of near-perfect mode-matching, which are not shown, revealed a similar functional form to those shown in Figure 5, but with a lower minimum loss, which occurred at smaller L_{rt}.

5. EXPERIMENTAL REALIZATION

A measured photon decay time for a square, TIR-ring cavity with a round-trip path length of L_{rt}=2.11 cm is shown in Figure 6. The cavity was fabricated from fiber-optic grade-fused silica. The gap widths between the input and output couplers and the cavity were piezoelectrically controlled and monitored by interferometry. An excimer-pumped, dye laser was used as the source, which provided 0.15 mJ, ~20ns pulses at 620 nm and the output was detected with photomultiplier tube. A photon decay time of 1.8 μs was obtained, which corresponds to a round-trip loss of 55 ppm, which agrees with the theoretical maximum within experimental error. Based on a minimum detectable decay time change of $\Delta\tau/\tau$=0.004, this provides a minimum detectable absorption of ~0.2 ppm.

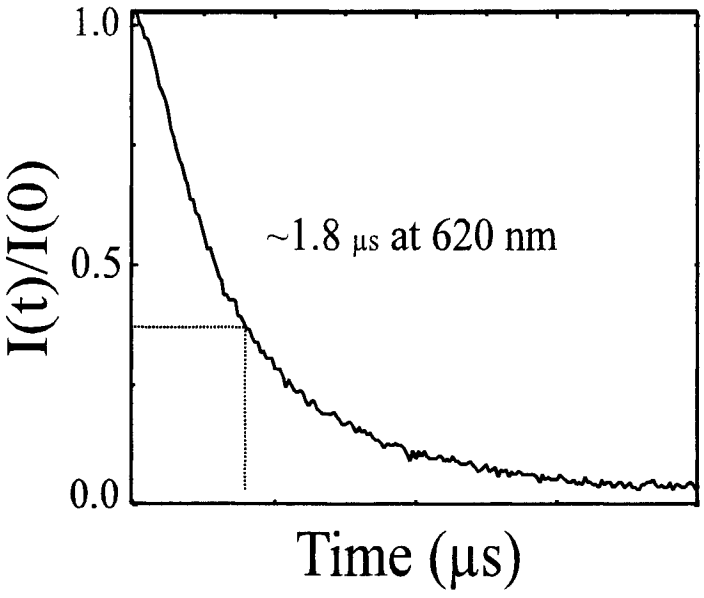

Figure 6. A plot of intensity versus time yields the photon decay time of 1.8 μs at 620 nm for a square TIR-ring cavity as depicted in Figure 4. This yields a round-trip loss of ~55 ppm. With $\Delta\tau/\tau$=0.004, this provides a minimum detectable absorbance change of ~0.2 ppm.

6. REFERENCES

1. A. O'Keefe and D. A. G. Deacon, Rev. Sci. Instrum. **59**, 2544 (1988).
2. A. C. R. Pipino, J. W. Hudgens, and R. E. Huie, Rev. Sci. Instrum.,**68** (8), 2978 (1997).
3. A. C. R. Pipino, J. W. Hudgens, and R. E. Huie, Chem. Phys. Lett., **280**, 104 (1997).
4. P. Zalicki and R. N. Zare, J. Chem. Phys. **102**, 2708, (1995).
5. J. J. Regan and D. R. Andersen, Comp. Phys. Jan/Feb. **49**, (1991).
6. N. J. Harrick, *Internal Reflection Spectroscopy*, (Interscience Publishers, New York, 1967).
7. I. N. Court and F. K. Von Willisem, Appl. Opt. **3**, 719. (1964).
8. M. W. Jones and K. C. Kao, J. Phys. E **2**, 331, (1969).
9. O. Kienzle, J. Staub, and T. Tschudi, Meas. Sci. Tech. **5**, 747, (1994).
10. An. N. Nesmeyanov, *Vapour Pressure of the Elements*, (Academic Press, New York 1963).
11. G. Kortum and H. Koffer, Ber. Bunsenges. Phys. Chem., **67**, 67, (1963).
12. J. G. Calvert and J. N. Pitts, Jr., *Photochemistry*, (John Wiley & Sons, New York, 1967).
13. *Fluoride Glass Fiber Optics*, Eds. I.D. Aggarwal and G. Lu, (Academic Press, Boston, 1991).
14. A. E. Seigman, *Lasers*, (University Science Books: Mills Valley, CA, 1986).
15. K. K. Lehmann and D. Romanini, J. Chem. Phys. **105**, 10263, 1996.
16. J. T. Hodges, J. P. Looney, R. D. Van Zee, J. Chem. Phys. **105**, 10278, 1996.

7. ACKNOWLEDGMENTS

This work was supported by the U.S. Department of Energy Environmental Management Science Program under contract 60231 and by internal NIST funding.

8. Disclaimer

Identification of specific commercial products in this paper is provided in order to specify procedures completely. In no case does such identification imply recommendation or endorsement by the National Institute of Standards and Technology, nor does it imply that such products have necessarily been identified as the best available for the purpose.